

The Physical Drivers of the Luminosity-Weighted Dust Temperatures in High-Redshift Galaxies

ANNE D. BURNHAM,¹ CAITLIN M. CASEY,¹ JORGE A. ZAVALA,¹ SINCLAIRE MANNING,¹ JUSTIN S. SPILKER,¹ PETER CAPAK,² SCOTT C. CHAPMAN,³ CHIAN-CHOU CHEN,⁴ ASANTHA COORAY,⁵ CHRISTOPHER HAYWARD,⁶ DAVID B. SANDERS,⁷ NICK Z. SCOVILLE,⁸ AND KARTIK SHETH⁹

¹Department of Astronomy, The University of Texas at Austin, 2515 Speedway Blvd Stop C1400, Austin, TX 78712, USA

²Infrared Processing and Analysis Center, California Institute of Technology, Pasadena, CA 91125, USA

³Department of Physics and Atmospheric Science, Dalhousie University, 6310 Coburg Road, Halifax, Nova Scotia, B3H 4R2, Canada

⁴European Southern Observatory, Karl Schwarzschild Strasse 2, Garching, Germany

⁵Center for Cosmology, Department of Physics and Astronomy, University of California, Irvine, CA 92697, USA

⁶Center for Computational Astrophysics, Flatiron Institute, 162 Fifth Avenue, New York, NY 10010, USA

⁷Institute for Astronomy, University of Hawaii at Manoa, 2680 Woodlawn Drive, Honolulu, HI 96822, USA

⁸California Institute of Technology, 1216 East California Boulevard, Pasadena, CA 91125, USA

⁹NASA Headquarters Washington DC 20546-0001, USA

(Received; Revised; Accepted)

Submitted to

ABSTRACT

The underlying distribution of galaxies' evolving dust SEDs (i.e. their spectra re-radiated by dust from rest-frame $\sim 3 \mu\text{m} - 3 \text{mm}$) remains relatively unconstrained due to a dearth of FIR/(sub)mm data for large samples of galaxies. It has been claimed in the literature that a galaxy's dust temperature—observed as the wavelength where the dust SED peaks (λ_{peak})—is traced most closely by its specific star-formation rate or parameterized distance to the SFR– M_* relation (the galaxy main-sequence). We present 0.24'' resolved 870 μm ALMA dust continuum observations of seven $z = 1.4 - 4.6$ dusty star-forming galaxies (DSFGs) chosen to have a large range of well-constrained luminosity-weighted dust temperatures. We also draw on similar resolution dust continuum maps from ALESS from [Hodge et al. 2016](#). We constrain dust continuum morphology and the physical scales over which the dust radiates and compare those measurements to characteristics of the integrated SED. The effective radii (R_e) of these galaxies range from 1.6 – 7.7 kpc. Their morphology is well-fit to a Gaussian profile (Sersic index $n = 0.62^{+0.11}_{-0.01}$). We confirm significant correlations of λ_{peak} —which is our adopted observational proxy for the luminosity-weighted dust temperature, T_d —with both L_{IR} (or SFR) and $L_{\text{IR}} R_e^{-2}$ (SFR surface density). Using a galaxy-scale Stefan-Boltzmann argument for the relationship between incident radiation heating dust in the ISM, we investigate the correlation between $\log_{10}(\lambda_{\text{peak}})$ and $\log_{10}(L_{\text{IR}} R_e^{-2})$. We find a value of the slope of this relation, $\eta = -0.22 \pm 0.01$, which deviates from the theoretical value of -0.25 by 2.6σ . The correlations of λ_{peak} with specific SFR (sSFR) and distance from the SFR– M_* relation (the galaxy main sequence) are less significant than those for L_{IR} or $L_{\text{IR}} R_e^{-2}$; therefore, we conclude that the more fundamental tracer of galaxies' luminosity-weighted integrated dust temperatures are indeed their star-formation surface densities.

Keywords: dust, galaxies: evolution, galaxies: starburst, galaxies: high-redshift, infrared: galaxies

1. INTRODUCTION

Dusty Star-Forming Galaxies (DSFGs) have incredibly high star-formation rates and produce $\sim 50\%$ of the stellar mass in the Universe in the first few Gyr. They are vitally important to galaxy evolution, but many of their fundamental dust characteristics are not well studied. Though their far-infrared through millimeter spec-

tral energy distributions (SEDs) are relatively straightforward to interpret as a linear combination of modified blackbodies from dust, which re-radiates nascent starlight, the lack of detailed photometry along that SED (rarely exceeding a few measurements across a 1000 μm range) has limited our understanding of the physics governing that dust in the interstellar medium

(ISM). This includes the physical scales over which the dust radiates and how clumpy it is, perhaps tracing back to its origins in/around compact star clusters. Physically tracing the relationship between integrated SEDs and underlying geometry is critically important.

A major challenge in characterizing galaxies' dusty SEDs has been the fundamental limitation of infrared through radio datasets, particularly for high- z galaxies. For ten years before 2010 most analysis was limited to SCUBA flux densities along the Rayleigh-Jeans tail of blackbody emission, which made it impossible to constrain both the IR luminosity and dust temperature of a given high- z galaxy. Even the vast improvement ushered in by *Herschel* in the last decade has fundamental limitations given the telescope's enormous beamsize at $250\,\mu\text{m}$ – $500\,\mu\text{m}$, where SEDs of $z = 1$ – 3 galaxies peak. The uncertainty brought on by confusion noise, added with the relatively shallow depth of *Herschel* surveys provides some moderate breakthroughs in measuring galaxies' dust temperatures across cosmic time.

Dust temperature is observationally constrained through measurement of λ_{peak} , the wavelength at which the SED peaks, which is inversely proportional to the underlying physical dust temperature via Wien's law (Wien 1897). The precise mapping of λ_{peak} to T_d depends on the underlying opacity of the dust in the ISM (see Figure 20 of Casey et al. (2014)) and is usually unconstrained without spatially-resolved observations. datasets have shown us that DSFGs at all epochs have higher temperatures at higher IR luminosities (e.g. Casey, Narayanan, & Cooray 2014 Blain et al. 2004, Ulza, Perault 1987). This relationship is akin to a Stefan-Boltzmann law for the cold ISM on galaxy scales. An evolution of integrated dust temperature has been observed between local and high- z DSFGs such that higher- z sources have colder dust, which is credited possibly to more extended dust geometries (Casey et al. 2012; Symeonidis et al. 2013; Lee et al. 2013; Kirkpatrick et al. 2017). Further investigation shows that this evolution may only exist at $z < 0.4$, though further work is required to determine whether this evolution is physically real or due to a selection bias (Casey et al. 2018a, Drew et al. in preparation).

Dust is heated by radiation with an intensity represented by U . The dust is heated in two environments: the diffuse ISM and photo-dissociation regions. The portion in the ISM is heated by a radiation field with constant U_{min} , and the other portion is heated by more direct starlight with intensities ranging from U_{min} and U_{max} (Magdis et al. 2012). The equation governing the dust-weighted mean starlight intensity scale factor, $\langle U \rangle$ is defined in Magdis et al. 2012. From this equation, $\langle U \rangle$

is proportional to $L_{\text{IR}}/M_{\text{dust}}$. A corollary is that the luminosity-weighted dust temperature correlates with $\langle U \rangle$ via the Stefan-Boltzmann Law. The stronger the radiation field, the higher the dust temperature. Similarly, the more compact the dust is around the source of incident radiation, the hotter the dust.

Magdis et al. 2012 used samples of *Herschel*-detected galaxies to argue that the galaxy IR-spectral energy distribution depends solely on $\langle U \rangle$ and is independent of sSFR and M_* . They also argue that $\langle U \rangle$ evolves with time such that main sequence galaxies further back in time had more intense radiation fields, or higher $\langle U \rangle$. They find that T_d evolves with time such that main sequence galaxies at higher z (out to $z \sim 2$) have warmer temperatures than those at $z = 0$. Note that this is not necessarily contradictory to the finding that $z \sim 2$ galaxies have colder SEDs than $z \sim 0$ galaxies of similar L_{IR} ; this is due to the dramatic evolution in the main sequence between these epochs.

Magnelli et al. (2014) used *Herschel* observations to propose stronger correlations of T_d with specific star formation rate (sSFR) and parameterized distance to the main sequence (D_{MS}) rather than with L_{IR} . The correlation is such that dust temperature is fixed for a fixed redshift and sSFR, implying that galaxies with a particular sSFR contain star-forming regions with similar $\langle U \rangle$. An increase in these star-forming regions results in the increase of SFR (star formation rate) with stellar mass (M_*). Since starbursts have higher SFRs than galaxies with equivalent masses on the main sequence, more intense radiation fields coupled with higher densities could cause the elevated dust temperatures (Magnelli et al. 2014).

In this paper, we have selected a sample of seven DSFGs with a wide range of measured dust temperatures and confirmed spectroscopic redshifts for high spatial-resolution submillimeter (submm) follow-up to directly test for correlation between dust temperature and other galaxy characteristic quantities. We use new resolved dust continuum maps from ALMA band 7 observations at $870\,\mu\text{m}$ of these seven DSFGs to investigate the hypothesis that dust temperature maps directly to other observable characteristics such as galaxy size, morphology, star-formation surface density, and sSFR. We also include eleven ALESS sources in our analysis from Hodge et al. (2016), whose observations and sample are similar, though slightly shallower observations for brighter targets. Section 2 describes sample selection and observations. Section 3 gives our calculations of key physical properties of the relevant DSFGs. In Section 4, we discuss our findings, and we provide our conclusions in Section 5. We assume a concordance cosmology

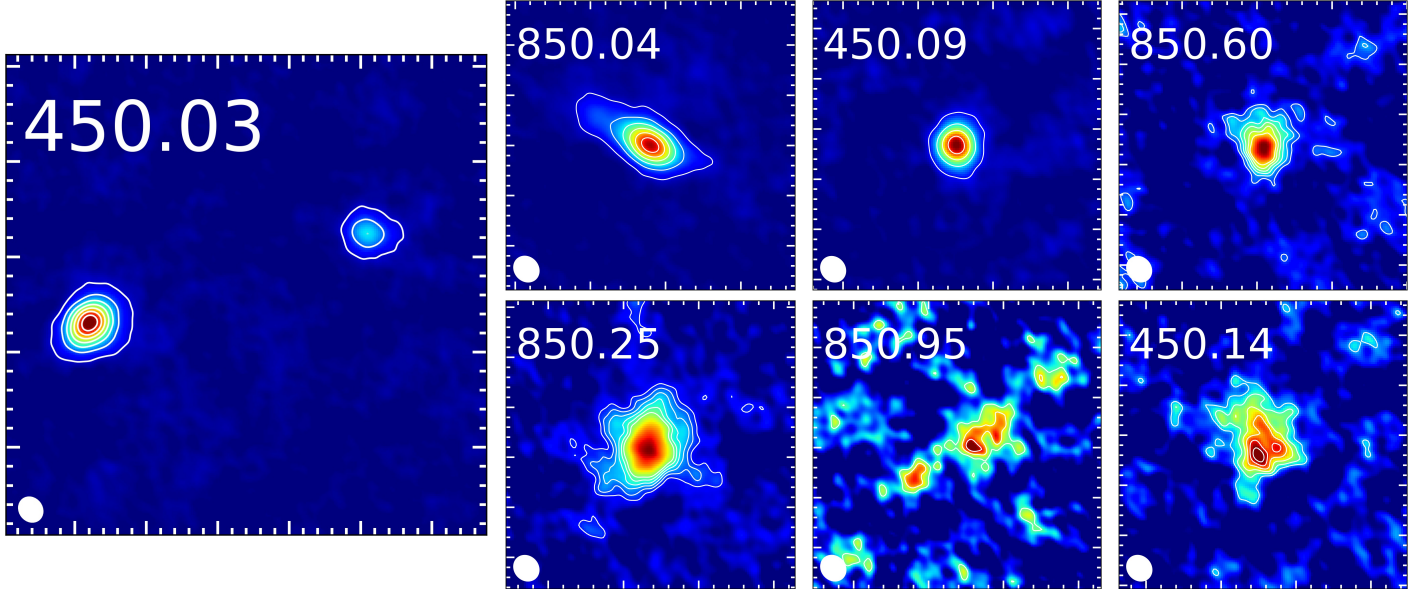


Figure 1. ALMA 870 μm images, proportional to the dust mass distribution. All images are $3'' \times 3''$, except for 450.03, which is $5'' \times 5''$ to show its two components (Jimenez-Andrade, submitted). The ALMA beam is shown in the bottom left corner. For sources 450.03, 850.04, and 450.09, the contours start at 5σ and increment by 10σ . For the remaining sources, the contours start at 2σ and increase by 1σ .

throughout this paper, adopting $H_0 = 70 \text{ km s}^{-1} \text{ Mpc}$, $\Omega_M = 0.3$, and $\Omega_\Lambda = 0.7$. Where SFRs are used, we assume a Chabrier IMF (Chabrier 2003).

2. SAMPLE AND OBSERVATIONS

2.1. Sample Selection

Seven unlensed, spectroscopically-confirmed SMGs were chosen from 400 arcmin 2 SCUBA-2 450 μm and 850 μm maps of the inner COSMOS field (Casey et al. 2013). These DSFGs were chosen for their relative brightness at 850 μm and for having known spectroscopic redshifts (Casey et al. 2017), which span $z = 1.4 - 4.6$. Of the SCUBA-2 detected COSMOS sample with spectroscopic redshifts, these seven sources were chosen to span a very broad range of dust SEDs from cold ($\sim 18\text{K}$) to warm ($\sim 70\text{K}$) based on their *Herschel* SPIRE and SCUBA-2 photometry. The galaxy initially thought to have the coldest SED, 450.03 (also known as AzTEC-2), was identified initially to have a spectroscopic redshift of 1.123 from an OIR counterpart (Casey et al. 2017) but is now confirmed to sit at $z = 4.63$ from a serendipitous detection of [CII] in our ALMA data and concurrent confirmation via CO(5-4) (Jimenez-Andrade et al. submitted). The ALMA centroid is offset from the OIR source by 1'' (see Casey et al. 2017 for details).

2.2. ALMA Data

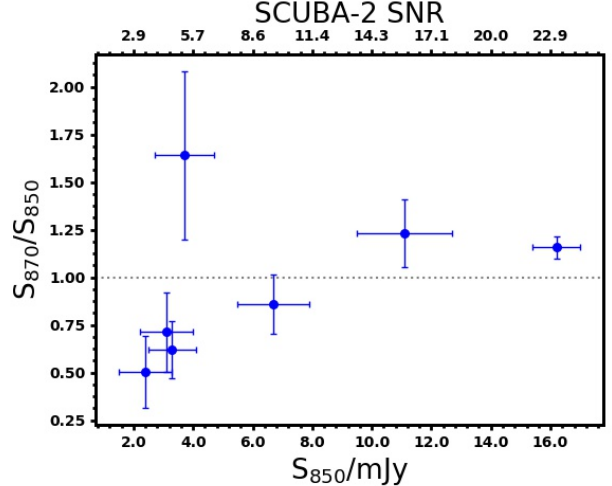


Figure 2. SCUBA flux (S_{850}) versus ratio of ALMA to SCUBA flux (S_{870}/S_{850}) for each galaxy. The SCUBA-2 SNR was calculated using $\sigma = 0.7 \text{ mJy}/\text{beam}$. Two of the sources (450.09 and 850.04) have higher ALMA flux densities than SCUBA-2 flux densities. The remaining sources have lower ALMA flux densities.

Observations of these seven DSFGs were carried out as part of the ALMA Cycle 3 program 2015.1.00568.S (PI Casey). With a requested spatial resolution of 0''.1, observations were made in both compact (configuration C36-3) and extended (configuration C36-6) configurations. The compact and extended configuration had

Table 1. Total flux densities, dust masses, half-light radii, peak wavelengths, infrared luminosities, and star formation rates for our seven COSMOS SCUBA-2 sources. Peak wavelengths, infrared luminosities, and star formation rates were also measured for eleven ALESS sources following the methodology of this paper. ALESS dust masses are from da Cunha et al. (2015), flux densities from Swinbank et al. (2014), and sizes from Hodge et al. (2016).

Name	S ₈₇₀	M _{dust}	R _e	λ _{peak}	L _{IR}	SFR
	[mJy]	[M _⊙]	[kpc]	[μm]	[L _⊙]	[M _⊙ /yr]
450.03	18.75 ± 0.15	(7.51 ± 0.06) × 10 ¹⁰	1.51 ± 0.14	63.6 ± 9.9	(3.3 ± 1.3) × 10 ¹³	-
850.04	13.67 ± 0.12	(1.46 ± 0.01) × 10 ¹⁰	2.79 ± 0.20	166 ± 30	(1.17 ± 0.64) × 10 ¹²	174 ± 96
450.14	2.05 ± 0.03	(2.37 ± 0.03) × 10 ⁹	2.88 ± 0.92	132 ± 32	(1.24 ± 0.94) × 10 ¹²	-
850.60	2.21 ± 0.04	(2.40 ± 0.04) × 10 ⁹	2.20 ± 0.67	76.5 ± 8.6	(1.91 ± 0.44) × 10 ¹²	282 ± 66
850.95	1.21 ± 0.03	(1.44 ± 0.04) × 10 ⁹	7.71 ± 3.73	98 ± 22	(1.22 ± 0.69) × 10 ¹²	182 ± 100
850.25	5.76 ± 0.05	(1.21 ± 0.01) × 10 ¹⁰	3.24 ± 0.47	110 ± 20	(3.1 ± 1.4) × 10 ¹²	457 ± 200
450.09	6.07 ± 0.07	(1.29 ± 0.01) × 10 ¹⁰	1.54 ± 0.14	70.9 ± 7.9	(8.3 ± 1.4) × 10 ¹²	1230 ± 210
ALESS 3.1	8.28 ± 0.40	(9.8 ^{+5.4} _{-4.5}) × 10 ⁸	2.18 ± 0.04	69.1 ± 8.7	(1.64 ± 0.25) × 10 ¹³	2455 ± 380
ALESS 5.1	7.78 ± 0.68	(1.20 ^{+0.66} _{-0.47}) × 10 ⁹	3.10 ± 0.08	106 ± 12	(4.90 ± 0.99) × 10 ¹²	733 ± 150
ALESS 9.1	8.75 ± 0.47	(7.1 ^{+6.5} _{-2.1}) × 10 ⁸	2.32 ± 0.04	70.9 ± 8.7	(1.63 ± 0.26) × 10 ¹³	2428 ± 390
ALESS 10.1	5.25 ± 0.50	(1.23 ^{+0.03} _{-0.40}) × 10 ⁹	2.85 ± 0.11	189.5 ± 8.6	(2.31 ± 0.37) × 10 ¹¹	34.5 ± 5.5
ALESS 15.1	9.01 ± 0.37	(2.5 ^{+1.0} _{-1.1}) × 10 ⁹	3.04 ± 0.06	125.2 ± 4.8	(2.95 ± 0.24) × 10 ¹²	440 ± 36
ALESS 17.1	8.44 ± 0.46	(2.14 ^{+0.69} _{-0.47}) × 10 ⁹	1.92 ± 0.03	137.9 ± 5.2	(1.88 ± 0.18) × 10 ¹²	281 ± 27
ALESS 29.1	5.90 ± 0.43	(5.8 ^{+2.3} _{-1.9}) × 10 ⁸	2.09 ± 0.04	136 ± 12	(1.37 ± 0.23) × 10 ¹²	204 ± 34
ALESS 39.1	4.33 ± 0.34	(1.07 ^{+0.32} _{-0.32}) × 10 ⁹	2.47 ± 0.04	99.7 ± 6.8	(3.26 ± 0.44) × 10 ¹²	487 ± 66
ALESS 45.1	6.03 ± 0.54	(8.5 ^{+4.3} _{-4.3}) × 10 ⁸	2.72 ± 0.09	117.4 ± 9.8	(2.67 ± 0.48) × 10 ¹²	399 ± 71
ALESS 67.1	4.50 ± 0.38	(7.4 ^{+3.2} _{-2.2}) × 10 ⁸	2.62 ± 0.11	72.2 ± 2.6	(9.42 ± 0.94) × 10 ¹²	1406 ± 140
ALESS 112.1	7.62 ± 0.49	(1.91 ^{+0.88} _{-0.83}) × 10 ⁹	2.94 ± 0.08	109.3 ± 5.7	(4.11 ± 0.47) × 10 ¹²	614 ± 70

maximum baselines of 462.9 m and 1.8 km, respectively, with 36 antennas. The observations targeted dust continuum emission at the nominal band 7 frequency centered at 345 GHz or 870 μm. At this frequency, ALMA has a 17."3 primary beam (FWHM), and we utilized the single continuum spectral mode.

We reduced and calibrated the raw data from the compact configuration to produce *uv*-data products using the Common Astronomy Software Applications (CASA) version 4.5.3. During calibration, data from antennas with irregular amplitudes were flagged. To produce optimum images for total flux recovery, we imaged the compact-configuration data using the CLEAN algorithm of CASA with Briggs weighting and robust = 2 (equivalent to natural weighting) and applied a primary beam correction. The resulting images have a resolution of 0".68 × 0".49. The compact data set was used in calculating the flux densities and dust masses, which are given in Table 1.

We created a higher resolution set of maps by combining the raw data from the compact and extended configurations, then reducing and calibrating the data using the same method described above. We tested different robust values with the CLEAN algorithm and found the

resulting size of each source to be consistent at independent of the robust parameter. Thus, we adopt a robust value of 1 for the full sample as it maximizes the source signal-to-noise for the most extended source in the sample (850.95). The resulting resolution is 0'.27 × 0'.24. The combined data was used to calculate the effective radii, which are also given in Table 1. The data was also imaged as seen in Figure 1.

3. METHODS

3.1. Flux density

Total integrated flux densities were measured directly from the compact ALMA data using a method similar to the one described in Hodge et al. (2016). We converted the maps from Jy beam⁻¹ to mJy pixel⁻¹ and masked flux emissions less than 2σ. We then summed contiguous emissions within an aperture of radius 3 × b_{maj} , where b_{maj} is the FWHM (major axis) of the synthesized beam. The resulting total band 7 flux densities are given in Table 1.

In general, when measuring the flux density, only contiguous emissions were summed, with one exception. Source 450.03 is composed of two sources separated by

3" at the same redshift (Jimenez-Andrade et al. submitted), both of which were included in the flux density.

To check our flux density calculations, we used the IMFIT tool in CASA and found that our calculations agree with the IMFIT-derived densities for all but three of our sources. Sources 850.60 and 850.95 differed with a less than 2σ significance of deviation. The average ratio between IMFIT and aperture flux density measurements was 0.96 ± 0.10 .

In addition, we compare the flux densities as measured by ALMA to the flux densities obtained from SCUBA-2 at $850\mu\text{m}$ using the single-dish JCMT. The average ratio of ALMA to SCUBA-2 flux densities was 0.86 ± 0.20 , as shown in Figure 2.

3.2. Dust emission morphology

To quantitatively examine the size of the emission, we begin by fitting a two-dimensional Sersic model to each source. Dust emission half-light effective radii were measured using GALFIT on the ALMA maps in the image plane. GALFIT is a 2D fitting tool that models the profiles of astronomical objects using parametric functions (Peng et al. 2010). Here we use GALFIT on ALMA data to test for non-Gaussian source morphologies, which is most easily applied in the image plane. Most of our sources are moderately resolved—more than 2 beams across in size—so size measurements are unlikely to be affected by fitting methods. Thus, making measurements in the image plane rather than the uv plane is justified.

To address whether the weighting applied with the CLEAN algorithm has an impact on size measurement in the image plane, measurements were also made in the uv plane. The measured sizes in the uv plane are systematically offset from the measured sizes in the image plane in a consistent manner for the full sample. Our scientific results rely on relative size comparisons of objects within the sample (and extended to the ALESS sample) rather than absolute sizes and therefore, for consistency, we base our analysis on image-plane measured sizes.

The results of GALFIT are shown in Figure 3 along with the residuals and models. The effective radii (R_e) range from $0''.19$ – $0''.90$ with a median of $R_e = 0''.33 \pm 0''.07$. Using the spectroscopic redshift of each source, we convert these angular sizes to physical sizes, which range from 1.5 – 7.7 kpc (median $R_e = 2.8 \pm 0.6$). Source 850.95 was an outlier at 7.7 ± 0.15 kpc. It is known to be somewhat abnormally large as also traced by H α kinematics (Drew et al. 2018). The remaining sources ranged from 1.5 – 3.2 kpc (median $R_e = 2.2 \pm 0.7$ kpc).

The median size of our sources is consistent with that of the ALESS sources in Hodge et al. (2016) measured

via the same technique, where the median $R_e = 1.8 \pm 0.2$ kpc despite the fact that the ALESS sample is consistently brighter. If we exclude our outlier, the median size of our sample agrees with the median size of the ALESS sources. Overall, the DSFG population from which the ALESS and COSMOS SCUBA-2 DSFGs are drawn are very similar, with the exception of their total $870\mu\text{m}$ flux densities being $1.3\times$ brighter.

The Sersic indices of our sources range from 0.38 to 0.76, with a median of $n = 0.62^{+0.11}_{-0.01}$. Only one galaxy had a Sersic index below 0.5, and noting that a Sersic fit with $n = 0.5$ is equivalent to a Gaussian fit, non-Gaussian morphologies are unlikely to be consistent with our sources. Our median n is weakly consistent with that of the ALESS sources in Hodge et al. (2016), whose median Sersic index $n = 0.9 \pm 0.2$ implies a non-Gaussian, exponential disk morphology.

Given the similarity of the median profile of our sources with a Gaussian profile, we choose to further investigate source morphology by fitting a two-dimensional Gaussian to each source in the image plane using the CASA tool IMFIT. The angular sizes (FWHMs deconvolved from the restoring beam) range from $0''.26$ – $1''.67$, which convert to 2.1 – 14.1 kpc on physical scales.

A comparison of the results of the two fitting methods is given in Table 2. From the table, it can be seen that for four of the sources (450.14, 850.60, 850.95, and 850.25), the Sersic profile fit is consistent with a Gaussian fit. The three that are inconsistent have low significance of deviation (2 – 3σ).

The median size of our sources agrees with molecular gas CO observations taken at high resolution, which concluded that SMGs have effective radii of $R_e = 2 \pm 1$ kpc, twice the physical size of local ULIRGs (e.g. Tacconi et al. 2008; Bothwell et al. 2010; Engel et al. 2010). Excluding the outlier, 850.95, the range of our sources' sizes are consistent with these findings.

3.3. Dust mass

We can directly derive dust masses from the submm flux density and dust temperature measurements using the following relationship:

$$S_\nu = \kappa_\nu B_\nu M_d D_L^{-2} \quad (1)$$

where S_ν is the flux density at frequency ν , κ_ν is the dust mass absorption coefficient at ν , B_ν is the Planck function defined at an average dust temperature T , M_d is the total dust mass, and D_L is the luminosity distance. This holds in the submm regime, where dust is optically thin. Following Scoville et al. (2016), we use $T = 25\text{K}$ for the mass-weighted dust temperature. We

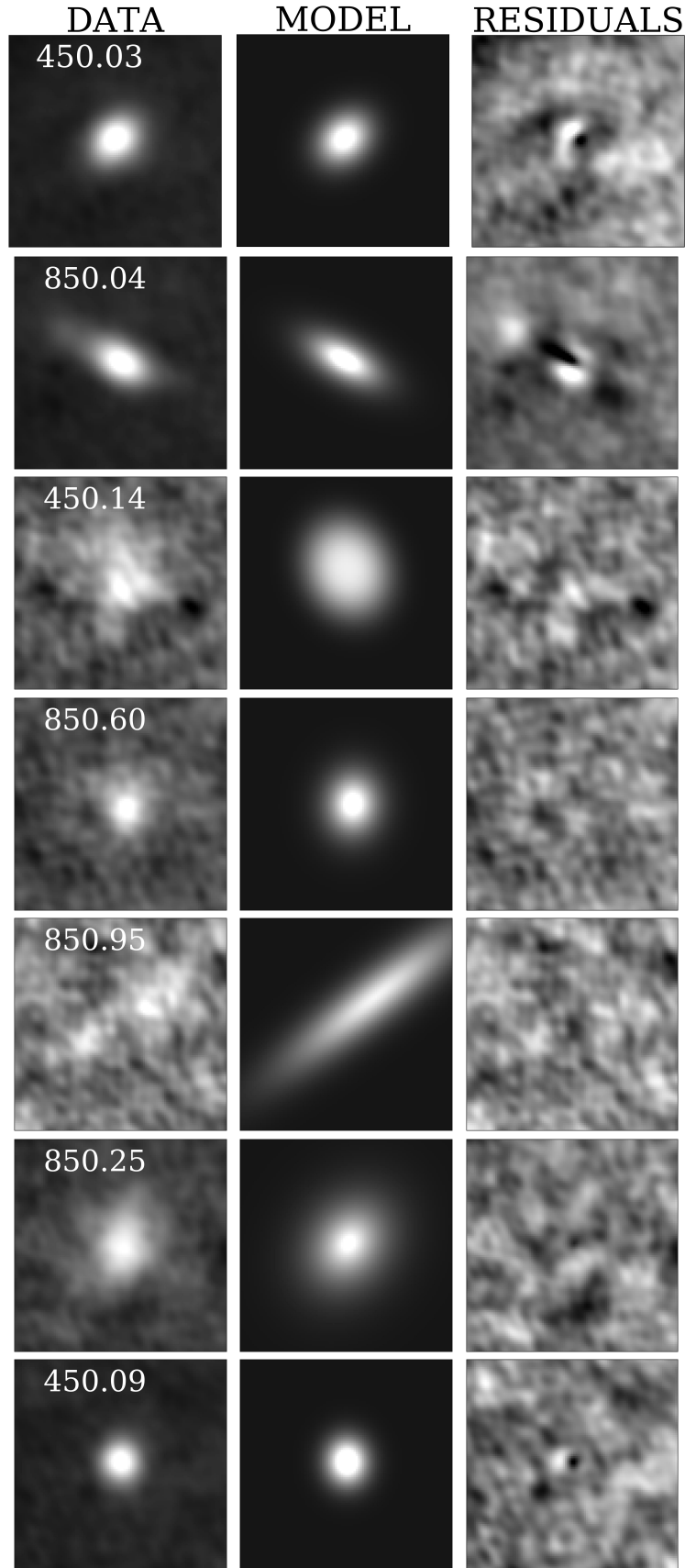


Figure 3. $4'' \times 4''$ model and residual images generated by GALFIT for each source. Images on the far left are the original ALMA 870 μm images with robust = 1.

Table 2. DSFG observed 870 μm dust morphologies. Measurements were made using the combined (compact and extended configuration) data. R_e is the effective (half-light) radius of the major axis from a two-dimensional Sersic profile fit. FWHM_{maj} is the FWHM of the major axis derived from a two-dimensional Gaussian fit in the image plane. n is the Sersic index from the two-dimensional Sersic profile fit.

Name	R_e	FWHM_{maj}	$2.02 \times R_e$	n
	[kpc]	[kpc]	[kpc]	
450.03	1.5 ± 0.14	2.5 ± 0.14	3.0 ± 0.28	0.6
850.04	2.8 ± 0.20	4.4 ± 0.20	5.7 ± 0.40	0.7
450.14	2.9 ± 0.92	5.5 ± 0.92	5.9 ± 1.9	0.4
850.60	2.2 ± 0.67	3.6 ± 0.67	4.4 ± 1.3	0.7
850.95	7.6 ± 3.7	14 ± 3.7	15 ± 7.3	0.6
850.25	3.2 ± 0.47	5.5 ± 0.47	6.5 ± 0.84	0.8
450.09	1.5 ± 0.14	2.1 ± 0.14	3.0 ± 0.28	0.6

use the measured dust absorption coefficient of $\kappa_{850} = 0.15 \text{ m}^2 \text{ kg}^{-1}$ (Weingartner & Draine 2001; Dunne et al. 2003), $\nu_{\text{obs}} = 345 \text{ GHz}$, and $\beta = 1.8$. The calculated dust masses for each of the DSFGs are shown in Table 1. These were calculated using data from the compact configuration, rather than the combined configuration, so that no flux is resolved out. The median dust mass for the sample is $\langle M_{\text{dust}} \rangle = (1.21 \pm 0.97) \times 10^{10} \text{ M}_\odot$.

3.4. Dust Temperature

Wien's Law states that $\lambda_{\text{peak}} = b/T_d$ (where $b = 2.898 \times 10^{-3} \text{ mK}$), but this relationship deviates depending on the opacity of the blackbody as shown in Figure 20 of Casey et al. (2014). Thus, we parameterize the luminosity-weighted dust temperature, T_d , instead as the observable, λ_{peak} , the wavelength where the dust spectral energy distribution (SED) peaks. SEDs were fitted using the technique described in Casey (2012), based on a single dust temperature modified blackbody fit with a mid-infrared power law shortward of $\sim 70 \mu\text{m}$ in the rest frame. We adopt a general opacity model such that $\tau = 1$ at $200 \mu\text{m}$ following Conley et al. (2011). Though the opacity is unconstrained, λ_{peak} is largely insensitive to opacity assumptions. The measured peak wavelengths are given in Table 1. We also re-fit SEDs for the ALESS sources described in Hodge et al. (2016) whose multiwavelength photometry is given in Swinbank et al. (2014). Fitting SEDs for both the COSMOS SCUBA-2 DSFGs and the ALESS sources was done in a fully consistent manner.

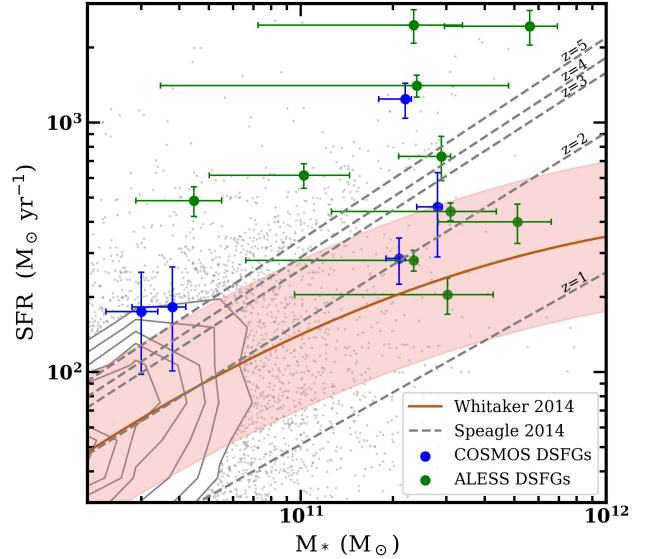


Figure 4. Five of our COSMOS sources (blue) and eleven ALESS sources (green) overplotted on the galaxy main sequence. The orange line is the best-fit polynomial of the form used in Whitaker et al. (2014) at $z = 2$, and the shaded region, with a width of 0.3 dex, represents the scatter of the main sequence. Sources within the shaded region lie on the main sequence. The dashed lines are the time-dependent best fits from Speagle (2014) for redshifts $z = 1, 2, 3, 4$, and 5.

3.5. Star Formation Rates and Stellar Masses

Star formation rates (SFRs) were calculated using the total infrared luminosities derived from the SED fits and the logarithmic constant of conversion, $\log(C_{\text{IR}}) = 43.41$ from Kennicutt & Evans (2012). We do not have reliable stellar mass estimates for 450.03 and 450.14 (see Casey et al. (2017), so they are omitted from all analysis requiring M_*). We used M_* values for our remaining five sources from Casey et al. (2017) and for the ALESS sources from da Cunha et al. (2015). We also calculated the specific star formation rate (sSFR), where $\text{sSFR} = \text{SFR} M_*^{-1}$.

Figure 3.5 shows the COSMOS and ALESS sources in relation to the SFR– M_* relation, also called the galaxy main sequence. We used MCMC techniques to fit the main sequence of star forming galaxies with a quadratic function of the form used in Whitaker et al. (2014) applied to COSMOS data from Laigle (2016). Shown also are the time-dependent best fits from Speagle (2014) for redshifts $z = 1, 2, 3, 4$, and 5.

4. DISCUSSION

Most galaxies for which dust temperatures have been constrained lack spatially-resolved measurements needed to investigate the effects of dust geometry on

dust temperature. Thus, the underlying physical driver of a galaxy's globally-averaged dust temperature has not been directly constrained. Before ALMA, there were small samples of high- z galaxies that had resolved radio or millimeter sizes (Chapman et al. 2004; Biggs & Ivison 2008; Casey et al. 2009; Younger et al. 2009), but the observations required to determine accurate sizes for larger samples of DSFGs require ALMA. In this paper, we have presented a sample of DSFGs, in combination with those brighter and well-studied DSFGs from ALESS, with both high resolution dust size constraints and good dust SED constraints, allowing a more thorough investigation into the origin of galaxies' dust SEDs.

This study is theoretically motivated by the application of the Stefan-Boltzmann law on galaxy scales. Specifically, it relates the emergent IR luminosity to the effective size R_e and temperature, T_d , of an optically thick blackbody:

$$L_{\text{IR}} = 4\pi R_e^2 \sigma T^4 \quad (2)$$

The Stefan-Boltzmann constant is $\sigma = 2.898 \times 10^{-3} \text{ m K}$. Though galaxies are certainly not as simple as stars in the application of such a relation, and dust in the ISM is not optically thick throughout (often far from it), it nevertheless would follow that a proportionality is expected, such that:

$$\log_{10}(\lambda_{\text{peak}}) \propto \eta \log_{10}\left(\frac{L_{\text{IR}}}{R_e^2}\right) \quad (3)$$

and the theoretical slope of this relation between $\log(\lambda_{\text{peak}})$ and $\log(L_{\text{IR}} R_e^{-2})$ is $\eta = -0.25$. $L_{\text{IR}} R_e^{-2}$ maps to the star-formation surface density of the galaxy.

Magnelli et al. (2014) report that T_d correlated more strongly with sSFR and parameterized distance to the main sequence (D_{MS}) than L_{IR} (they lacked direct measures of R_{eso} so could not investigate $L_{\text{IR}} R_e^{-2}$). In addition, they deduced that cold galaxies ($\lesssim 25\text{K}$) sit on the main sequence and warm galaxies ($\gtrsim 30\text{-}80\text{K}$) lie above the main sequence (Magnelli et al. 2014).

Here we investigate the relative strengths of correlations between λ_{peak} and each of sSFR, the parameterized distance to the main sequence, SFR, and $L_{\text{IR}} R_e^{-2}$. A linear model was fitted to the logarithm of each quantity using the Markov Chain Monte Carlo Method (MCMC). We calculate the significance of each correlation as the deviation of the model from a horizontal line in the given parameter space, which would indicate no correlation. The results are shown in Figure 5.

The models for the correlations of λ_{peak} with D_{MS} and sSFR both deviate from no correlation by 2σ . The

models of λ_{peak} with SFR and $L_{\text{IR}} R_e^{-2}$ deviate from no correlation by 24σ and 23σ , respectively. In addition, the slope $\eta = -0.22 \pm 0.01$ of the linear model for the $\log(\lambda_{\text{peak}})$ - $\log(L_{\text{IR}} R_e^{-2})$ relationship deviates from the theoretical value by just 2.6σ .

We find that the correlations of λ_{peak} with SFR (or L_{IR}) and star-formation surface density are statistically stronger than the correlations with D_{MS} and sSFR. We do not find evidence to support the theory that dust temperature correlates with a galaxy's position on the galaxy main sequence. Thus we infer that T_d is not necessarily a viable indicator of evolutionary class (starburst or quiescent disk) and that higher temperature does not necessarily indicate a starburst (Bothwell et al. 2010; Hodge et al. 2012, Drew in prep). In addition, ISM dust can be heated by AGN whether or not the galaxy hosts an ongoing starburst (Kirkpatrick et al. 2012). Additional recent cosmological simulation work supports the production of intense luminosities through secularly evolving disk systems (Davé et al. 2010; Hodge et al. 2012; Narayanan et al. 2015; Hayward et al. 2018; Tadaki et al. 2018).

That our slope α for the $\log(\lambda_{\text{peak}})$ - $\log(L_{\text{IR}} R_e^{-2})$ relationship is shallower than the theoretical -0.25 could be attributed to assumptions built into the application of the Stefan-Boltzmann Law to galaxies, namely that galaxy dust emission is a perfect blackbody and optically thick. Given that the slope of our model deviates from the theoretical value by 2.6σ , our results justify the generalization of the Stefan-Boltzmann Law to galaxy scales and inform the correlation of λ_{peak} (or T_d) with size. Casey et al. (2018b) modeled the $L_{\text{IR}}-\lambda_{\text{peak}}$ relationship by a power law such that in log-log space, $\log_{10}(\lambda_{\text{peak}}) \propto \eta \log(L_{\text{IR}})$. Through empirical measurement, they found $\eta = -0.068 \pm 0.001$. That the slope of their model, which does not include a size parameter as ours does, differs from our slope indicates a size dependency in the $\lambda_{\text{peak}}-L_{\text{IR}}$ relationship. Combining our model with theirs, we find that the size dependence can be modeled as a power-law function of L_{IR} such that $R_e \propto L_{\text{IR}}^{0.35}$. Using the same model (i.e., $\log_{10}(\lambda_{\text{peak}}) \propto \eta \log(L_{\text{IR}})$) as Casey et al. (2018b), Siebenmorgen & Krugel (2007) found $\eta \approx -0.16$, through radiative transfer modeling, using a spherically symmetric model accounting for different sizes, dust masses, and SFRs.

5. CONCLUSIONS

We used $0.24''$ resolved $870\mu\text{m}$ ALMA dust continuum observations to determine the total integrated flux density, dust mass, and size. We used SED fitting to determine λ_{peak} and L_{IR} . We investigated correlations of dust temperature with four galaxy characteristics:

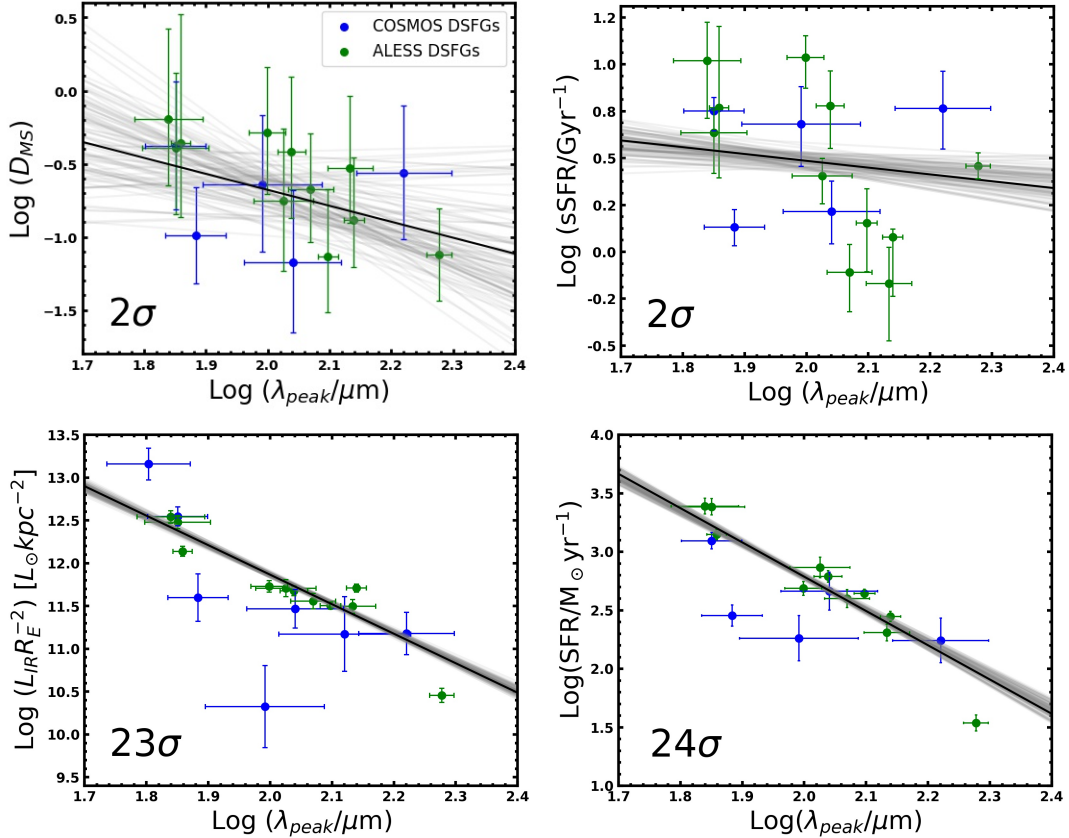


Figure 5. Correlations between λ_{peak} and the parameterized distance to the galaxy main sequence, sSFR, SFR, and $L_{\text{IR}} R_{\text{e}}^{-2}$. A linear model has been fitted in log – log space using MCMC techniques. A representative sample of MCMC trial fits shown in gray while the black line shows the best fit. The number in the lower left-hand corner of each plot represents the significance of the relation from a horizontal line, which would indicate no correlation. Larger numbers represent stronger correlations. We infer weak correlations of λ_{peak} with D_{MS} and sSFR and strong correlations of λ_{peak} with SFR and star formation surface density.

sSFR, parameterized distance to the galaxy main sequence, SFR, and star formation surface density. Our results are as follows:

- The morphology of our sources is well fit to a Gaussian profile, with an average Sersic index of $n = 0.62^{+0.11}_{-0.01}$. The R_{e} of our seven new DSFGs range from 1.6–7.7 kpc with sizes of the full sample analyzed at 870 μm with $\langle R_{\text{e}} \rangle = 2.8 \pm 0.6$ kpc.
- The median dust mass of our sources is $M_{\text{dust}} = (1.21 \pm 0.97) \times 10^{10} M_{\odot}$.
- The correlations of λ_{peak} with sSFR and D_{MS} are weak. The linear models relating $\log(\lambda_{\text{peak}})$ with $\log(\text{sSFR})$ and $\log(D_{\text{MS}})$ had a strength of only 2σ .
- The linear models relating $\log(\lambda_{\text{peak}})$ with $\log(\text{SFR})$ and $\log(L_{\text{IR}} R_{\text{e}}^{-2})$ had strengths of 24σ and 23σ , respectively, confirming that the $\lambda_{\text{peak}} - L_{\text{IR}}$ and $\lambda_{\text{peak}} - L_{\text{IR}} R_{\text{e}}^{-2}$ relationships are statistically

stronger than the $\lambda_{\text{peak}} - \text{sSFR}$ and $\lambda_{\text{peak}} - D_{\text{MS}}$ relationships.

We conclude that dust temperature is not necessarily an indication of where a galaxy sits on the main sequence and cannot be used to infer evolutionary class.

ADB thanks the John W. Cox Endowment for the Advanced Studies in Astronomy for support. CMC thanks the National Science Foundation for support through grants AST-1714528 and AST-1814034, and additionally CMC and JAZ thank the University of Texas at Austin College of Natural Sciences for support. In addition, CMC acknowledges support from the Research Corporation for Science Advancement from a 2019 Cottrell Scholar Award sponsored by IF/THEN, an initiative of Lyda Hill Philanthropies. This paper makes use of the following ALMA data: ADS/JAO.ALMA 2015.1.00568.S. ALMA is a partnership of ESO (representing its member states), NSF (USA) and NINS (Japan), together with NRC (Canada), MOST and

ASIAA (Taiwan), and KASI (Republic of Korea), in cooperation with the Republic of Chile. The Joint ALMA Observatory is operated by ESO, AUI/NRAO

and NAOJ. The National Radio Astronomy Observatory is a facility of the National Science Foundation operated under cooperative agreement by Associated Universities, Inc.

REFERENCES

- Biggs, A. D., & Ivison, R. J. 2008, MNRAS, 385, 893, doi: [10.1111/j.1365-2966.2008.12869.x](https://doi.org/10.1111/j.1365-2966.2008.12869.x)
- Blain, A. W., Chapman, S. C., Smail, I., & Ivison, R. 2004, ApJ, 611, 725, doi: [10.1086/422353](https://doi.org/10.1086/422353)
- Bothwell, M. S., Chapman, S. C., Tacconi, L., et al. 2010, MNRAS, 405, 219, doi: [10.1111/j.1365-2966.2010.16480.x](https://doi.org/10.1111/j.1365-2966.2010.16480.x)
- Casey, C. M. 2012, MNRAS, 425, 3094, doi: [10.1111/j.1365-2966.2012.21455.x](https://doi.org/10.1111/j.1365-2966.2012.21455.x)
- Casey, C. M., Hodge, J., Zavala, J. A., et al. 2018a, ApJ, 862, 78, doi: [10.3847/1538-4357/aacd11](https://doi.org/10.3847/1538-4357/aacd11)
- Casey, C. M., Narayanan, D., & Cooray, A. 2014, PhR, 541, 45, doi: [10.1016/j.physrep.2014.02.009](https://doi.org/10.1016/j.physrep.2014.02.009)
- Casey, C. M., Zavala, J. A., Spilker, J., da Cunha, E., & Hodge, J. 2018b, ApJL, doi: [10.3847/1538-4357/aac82d](https://doi.org/10.3847/1538-4357/aac82d)
- Casey, C. M., Chapman, S. C., Beswick, R. J., et al. 2009, MNRAS, 399, 121, doi: [10.1111/j.1365-2966.2009.15291.x](https://doi.org/10.1111/j.1365-2966.2009.15291.x)
- Casey, C. M., Berta, S., Béthermin, M., et al. 2012, ApJ, 761, 140, doi: [10.1088/0004-637X/761/2/140](https://doi.org/10.1088/0004-637X/761/2/140)
- Casey, C. M., Chen, C.-C., Cowie, L. L., et al. 2013, MNRAS, 436, 1919, doi: [10.1093/mnras/stt1673](https://doi.org/10.1093/mnras/stt1673)
- Casey, C. M., Cooray, A., Killi, M., et al. 2017, ApJ, 840, 101, doi: [10.3847/1538-4357/aa6cb1](https://doi.org/10.3847/1538-4357/aa6cb1)
- Chabrier, G. 2003, PASP, 115, 763, doi: [10.1086/376392](https://doi.org/10.1086/376392)
- Chapman, S. C., Smail, I., Windhorst, R., Muxlow, T., & Ivison, R. J. 2004, ApJ, 611, 732, doi: [10.1086/422383](https://doi.org/10.1086/422383)
- Conley, A., Cooray, A., Vieira, J. D., et al. 2011, ApJL, 732, L35, doi: [10.1088/2041-8205/732/2/L35](https://doi.org/10.1088/2041-8205/732/2/L35)
- da Cunha, E., Walter, F., Smail, I. R., et al. 2015, ApJ, 806, 110, doi: [10.1088/0004-637X/806/1/110](https://doi.org/10.1088/0004-637X/806/1/110)
- Davé, R., Finlator, K., Oppenheimer, B. D., et al. 2010, MNRAS, 404, 1355, doi: [10.1111/j.1365-2966.2010.16395.x](https://doi.org/10.1111/j.1365-2966.2010.16395.x)
- Drew, P. M., Casey, C. M., Burnham, A. D., et al. 2018, apj, 869, 6, doi: [10.3847/1538-4357/aaedbf](https://doi.org/10.3847/1538-4357/aaedbf)
- Dunne, L., Eales, S., Ivison, R., Morgan, H., & Edmunds, M. 2003, Nature, 424, 285, doi: [10.1038/nature01792](https://doi.org/10.1038/nature01792)
- Engel, H., Tacconi, L. J., Davies, R. I., et al. 2010, ApJ, 724, 233, doi: [10.1088/0004-637X/724/1/233](https://doi.org/10.1088/0004-637X/724/1/233)
- Hayward, C. C., Chapman, S. C., Steidel, C. C., Golob, A., & Casey, C. M. 2018, MNRAS, 476, 2278, doi: [10.1093/mnras/sty304](https://doi.org/10.1093/mnras/sty304)
- Hodge, J. A., Carilli, C. L., Walter, F., et al. 2012, ApJ, 760, 11, doi: [10.1088/0004-637X/760/1/11](https://doi.org/10.1088/0004-637X/760/1/11)
- Hodge, J. A., Swinbank, A. M., Simpson, J. M., et al. 2016, ApJ, 833, 103, doi: [10.3847/1538-4357/833/1/103](https://doi.org/10.3847/1538-4357/833/1/103)
- Kennicutt, R. C., & Evans, N. J. 2012, ARA&A, 50, 531, doi: [10.1146/annurev-astro-081811-125610](https://doi.org/10.1146/annurev-astro-081811-125610)
- Kirkpatrick, A., Pope, A., Alexander, D. M., Charmandaris, V., & Daddi, E. 2012, ApJ, 759, 23, doi: [10.1088/0004-637X/759/2/139](https://doi.org/10.1088/0004-637X/759/2/139)
- Kirkpatrick, A., Pope, A., Sajina, A., et al. 2017, ApJ, 843, 71, doi: [10.3847/1538-4357/aa76dc](https://doi.org/10.3847/1538-4357/aa76dc)
- Laigle, C., M. H. J. I. O. H. B. C. 2016, apj, 224, 24
- Lee, N., Sanders, D. B., Casey, C. M., et al. 2013, ApJ, 778, 131, doi: [10.1088/0004-637X/778/2/131](https://doi.org/10.1088/0004-637X/778/2/131)
- Magdis, G. E., Daddi, E., Béthermin, M., et al. 2012, ApJ, 760, 6, doi: [10.1088/0004-637X/760/1/6](https://doi.org/10.1088/0004-637X/760/1/6)
- Magnelli, B., Lutz, D., Saintonge, A., et al. 2014, A&A, 561, A86, doi: [10.1051/0004-6361/201322217](https://doi.org/10.1051/0004-6361/201322217)
- Narayanan, D., Turk, M., Feldmann, R., et al. 2015, Nature, 525, 496, doi: [10.1038/nature15383](https://doi.org/10.1038/nature15383)
- Peng, C. Y., Ho, L. C., Impey, C. D., & Rix, H.-W. 2010, AJ, 139, 2097, doi: [10.1088/0004-6256/139/6/2097](https://doi.org/10.1088/0004-6256/139/6/2097)
- Scoville, N., Sheth, K., Aussel, H., Vanden Bout, P., & Capak, P. 2016, ApJ, 820, 21, doi: [10.3847/0004-637X/820/2/83](https://doi.org/10.3847/0004-637X/820/2/83)
- Siebenmorgen, R., & Krugel, E. 2007, A&A, 461, 445, doi: [10.1051/0004-6361:20065700](https://doi.org/10.1051/0004-6361:20065700)
- Speagle, J. S., S. C. L. C. P. L. S. J. D. 2014, ApJ, 214, 52, doi: [10.1088/0067-0049/214/2/15](https://doi.org/10.1088/0067-0049/214/2/15)
- Swinbank, A. M., Simpson, J. M., Smail, I., et al. 2014, MNRAS, 438, 1267, doi: [10.1093/mnras/stt2273](https://doi.org/10.1093/mnras/stt2273)
- Symeonidis, M., Vaccari, M., Berta, S., et al. 2013, MNRAS, 431, 2317, doi: [10.1093/mnras/stt330](https://doi.org/10.1093/mnras/stt330)
- Tacconi, L. J., Genzel, R., Smail, I., et al. 2008, ApJ, 680, 246, doi: [10.1086/587168](https://doi.org/10.1086/587168)
- Tadaki, K., Iono, D., Yun, M. S., et al. 2018, Nature, 560, 613, doi: [10.1038/s41586-018-0443-1](https://doi.org/10.1038/s41586-018-0443-1)
- Weingartner, J. C., & Draine, B. T. 2001, ApJ, 548, 296, doi: [10.1086/318651](https://doi.org/10.1086/318651)
- Whitaker, K. E., Franx, M., Leja, J., et al. 2014, ApJ, 795, 104, doi: [10.1088/0004-637X/795/2/104](https://doi.org/10.1088/0004-637X/795/2/104)
- Wien, W. 1897, The London, Edinburgh, and Dublin Philosophical Magazine and Journal of Science, 43, 214, doi: [10.1080/14786449708620983](https://doi.org/10.1080/14786449708620983)

Younger, J. D., Omont, A., Fiolet, N., et al. 2009, MNRAS,
394, 1685, doi: [10.1111/j.1365-2966.2009.14455.x](https://doi.org/10.1111/j.1365-2966.2009.14455.x)